An efficient algorithm for microtubule-based nucleation reveals large sensitivity to cell geometry of the plant cortical array

Marco Saltini, Eva E. Deinum

Mathematical & Statistical Methods (Biometris), Plant Science Group, Wageningen University, 6708 PB Wageningen, The Netherlands

Keywords: computational biology, plant cortical microtubules, nucleation, event-driven simulations, biophysical modelling, CorticalSim.

Abstract

Understanding how cortical microtubules self-organise into aligned arrays and how cell geometry influences this process is central to investigating many plant cell functions, including cell morphogenesis and anisotropic growth. Here, we focus on microtubule nucleation as a critical factor affecting array behaviour. Existing computational algorithms for microtubule nucleation are insufficiently realistic, which also results in less realistic behaviour of the whole array. Algorithms that do incorporate the fact that most nucleation occurs from existing microtubules, behave least realistic due to computational artefacts. This results in severely inhomogeneous cortical arrays, characterized by large empty spaces and few densely populated areas. In real cells, such arrays would be detrimental to cell wall integrity. We have developed a novel, more realistic algorithm that efficiently simulates microtubule nucleation via approximating the diffusion of nucleation complexes at the membrane. This algorithm supports uniform arrays by maintaining realism in the nucleation process without the computational burden of explicit diffusion simulation. To demonstrate the importance of sufficiently realistic microtubule nucleation, we compared our novel algorithm with existing nucleation algorithms. We observed large differences among algorithms in preferred array orientation. We found that the enhanced biological realism of the nucleation process strongly increased the tendency to adopt a transverse orientation on cylindrical cells. This finding has important implications for the ongoing debate about how array orientation is controlled. Our approach opens up new avenues for quantitative comparisons of different factors influencing array behaviour, including orientation and patterning.

Introduction

Plants take their shape through coordinated processes of cell division, expansion and differentiation. At the cellular level, many of these processes are shaped by the plant cortical microtubule array [1–3]. This dynamic structure of membrane associated microtubules guides the anisotropic deposition of cellulose microfibrils, the main load bearing component of the cell wall, and predicts the future cell division site [4–7]. Under the right conditions [8, 9], these dynamic microtubules can self-organise into a highly aligned array. This self-organisation depends on frequent collisional interactions among microtubules, resulting in angle-dependent outcomes [10]. The dynamics of individual microtubules, by controlling the strength of such collisional interactions, play a crucial role in this organisation [8, 11]. Microtubule nucleation, particularly the orientation of newly-generated microtubules in relation to their parent microtubules, has a profound impact on the self-organisation of the cortical microtubule array and its ability to adopt complex patterns [12–17]. Consequently, any quantitative predictions from computer simulations critically depend on the sufficiently realistic implementation of microtubule nucleation.

This is particularly relevant in the ongoing debate about what controls the orientation of the cortical microtubule array. Array orientation is significantly influenced by a combination of global and local cues. For example, global cues such as cell geometry can favour array orientation along the shortest closed circumferences of the cell [18, 19]. Local cues, including the alignment of microtubules with mechanical stresses [20], could select for a specific orientation among these, or potentially even override the global cues [21, 22]. Given that new microtubules in plants typically nucleate in directions strongly correlated with the orientation of their parent microtubule [16, 17, 23], how microtubules are nucleated in simulations of the cortical array is crucial. Indeed, different nucleation modes result in different sensitivities to local and global cues [12, 13, 22, 24]. Therefore, the ability to realistically simulate microtubule nucleation is critical for any computational study that involves a competition between local and global cues affecting alignment and orientation.

Despite this importance, however, most computational research on microtubule arrays has traditionally employed isotropic nucleation, where microtubules are initiated at random positions with random orientations. While helpful for understanding the effects of microtubule collisions [8, 10, 25] and geometrical constraints on alignment [18, 21, 26–28], this approach ignores that microtubules often nucleate from existing ones [15, 23, 29]. Many simulation studies with microtubule-based nucleation [13, 16, 30, 31], however, suffer from a so-called "inhomogeneity problem" [12]. In essence, this is a computational problem arising from a naive implementation of microtubule-based nucleation, i.e., when microtubule-based nucleation is linearly density-dependent. This density-dependence causes a positive feedback on local microtubule density, leading to overly dense regions and very sparse areas in between. As cellulose synthase complexes are preferentially inserted near microtubules [6], such inhomogeneities would lead to structural weaknesses in the cell wall. While this feedback loop originates from the biological reality of microbule-based nucleation, the naive implementation has no force counteracting the positive feedback. In reality, however, the local nucleation rate saturates with density, thereby ensuring homogeneity [12].

Jacobs et al. [12] demonstrated that one solution to this problem is to explicitly consider the appearance and diffusion at the membrane of nucleation complexes. They implemented this in a simplified array simulation framework dubbed CorticalSimple, in which alignment of microtubules is taken for granted, i.e., they all have an exactly transverse orientation [12]. In CorticalSimple, nucleation complex diffusion takes up a large fraction the computational time, even though nucleation itself is a relatively rare event. The diffusion of explicit nucleation complexes is also employed in

CytoSim (e.g., [32]), in which the computational cost of diffusing "nucleators" is less problematic, because the microtubule model itself is computationally much more demanding due to its larger degree of mechanical realism. The computational load of CytoSim, however, makes it less suitable for simulating a large number of instances of plant cortical arrays. A different platform, CorticalSim, is specifically developed for this. Previous publications with CorticalSim heavily use its computational efficiency, which allows for accurate computation of ensemble statistics from many simulations combined with exploration of parameter space in relatively short time [5, 11, 13, 16, 18, 33]. Such efficiency not only allows for more robust conclusions, but also the investigation of different types of questions. The computational efficiency of CorticalSim stems from its adoption of an event-driven approach for microtubule dynamics and interaction, which updates the system following each event rather than at fixed time intervals [11,19]. To maintain the computational advantages of CorticalSim, it is, therefore, necessary to develop a new nucleation algorithm that 1) behaves sufficiently realistic, so it reproduces local density-dependent nucleation of new microtubules without causing array inhomogeneity, and 2) is computationally efficient.

To tackle these challenges, we have developed a novel nucleation algorithm for CorticalSim that efficiently simulates the diffusion of nucleation complexes in a simplified manner. Our approach increases the biological realism of microtubule-based nucleation, enabling the natural emergence of density-dependence from the nucleation process at both local and global scales. This nucleation preserves the alignment-promoting effect of microtubule-based nucleation, while overcoming the long-standing issue of inhomogeneity. Furthermore, we compare arrays produced by our algorithm with those generated through isotropic and previous global density-dependent nucleation modes. Our results show that the nucleation mode has a major impact on the responsiveness of the array to cues of different types. With our new nucleation algorithm, cell geometry has a much stronger impact on array orientation than with previous, less realistic nucleation modes. These findings have important consequences for our understanding of array orientation.

Methods

The new nucleation algorithm is implemented in CorticalSim, a fast, event based microtubule simulation platform written in C++ [11]. Table 1 summarizes model parameters and their default values.

Microtubule dynamics

The dynamics of microtubules comprises two main components: intrinsic dynamics and microtubule-microtubule interaction. We employed the Dogterom and Leibler model [35] to describes the intrinsic dynamics of individual microtubules augmented with hybrid treadmilling [36], see Figure 1A. Microtubules can be either in the growing state, where they extend at the plus-end with a growth speed of v^+, or in the shrinking state, where they retract their plus-end with a shrinkage speed of v^-. The minus-end of microtubules retracts at a treadmilling speed of v^{tm} independently of the state of the plus-end. Transitions between the growing and shrinking states, and *vice versa*, occur with catastrophe and rescue rates denoted as r_c and r_r, respectively.

When a growing microtubule plus end impinges on the lattice of another microtubule, the resulting type of interaction depends on the collision angle, comprised between 0° and 90°. For collision angles smaller than $\theta_c = 40°$, zippering occurs, causing the plus end to reorient alongside

Table 1: Default model parameters.

Parameter	Description	Value	Unit	Source
v^+	Growth speed	0.05	μm s^{-1}	[13]
v^-	Shrinkage speed	0.08	μm s^{-1}	[13]
v^{tm}	Treadmilling speed	0.01	μm s^{-1}	[13]
r_c	Catastrophe rate	variable	s^{-1}	
r_r	Rescue rate	0.001	s^{-1}	[13]
θ_c	Maximum collisional angle for bundling	40°	-	[10]
P_{cat}	Fraction of induced catastrophe after collision when $\theta > \theta_c$	0.5	-	[33]
r_n	Nucleation rate for ISO and GDD	0.001	μm^{-2} s^{-1}	[13]
r_{ins}	Complex appearance rate for LDD	0.0045	μm^{-2} s^{-1}	[34]
r_u	Per-complex unbound nucleation rate	0.002	s^{-1}	[34]
D	Diffusion coefficient of nucleation complexes	0.013	μm^2 s^{-1}	
N	Number of meta-trajectories for LDD	6	-	
R	Maximum meta-trajectory length for LDD	1.5	μm	
$P_{\mathrm{rej},b}$	Rejection probability for microtubule-based nucleation for LDD	0.76	-	[15]
$P_{\mathrm{rej},u}$	Rejection probability for unbound nucleation for LDD	0.98	-	[12]
$\rho_{1/2}$	Tubulin density at which half of nucleations are isotropic for GDD	0.1	μm^{-1}	[16]
f_{forward}	Nucleation probability along the parent for GDD and LDD	0.31	-	[16]
f_{backward}	Nucleation probability anti-parallel to the parent for GDD and LDD	0.07	-	[16]
f_{left}	Nucleation probability to the left of the parent for GDD and LDD	0.31	-	[16]
f_{right}	Nucleation probability to the right of the parent for GDD and LDD	0.31	-	[16]
ϵ	Ellipse eccentricity for GDD and LDD	0.89	-	[23]
θ_b	Mean branching angle for GDD and LDD	35°	-	[23]

the encountered microtubule. When the collision angle is wider than 40°, the impinging plus-end has a probability P_{cat} to undergo a collision-induced catastrophe, and a probability $1 - P_{\mathrm{cat}}$ to create a cross-over with the other microtubule, see Figure 1B. Microtubule bundles emerge as a result of the zippering process. We assume that the collision between a growing microtubule tip and a bundle is equivalent to a collision with a single microtubule. Likewise, when a microtubule within a bundle collides with another microtubule, it remains unaffected by the presence of other microtubules within the same bundle. CorticalSim can simulate microtubule severing events induced by the severing enzyme katanin [33]. However, for simplicity, we do not consider katanin severing in this manuscript.

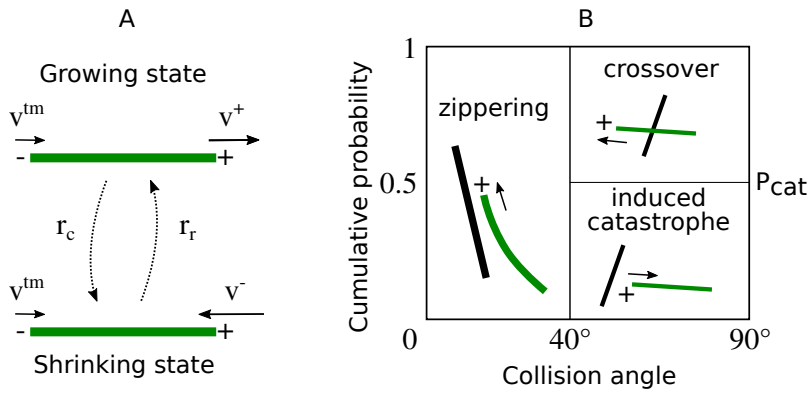

Figure 1: Schematic of the dynamics of individual microtubules. (A) Microtubules switch from periods of growth to periods of shrinkage (with catastrophe rate r_c), and *viceversa* (with rescue rate r_r). (B) Microtubule plus-ends impinging on the lattice of other microtubules with an angle lower than 40° result in zippering. For higher collision angles the result is an induced catastrophe of the impinging microtubule with probability P_{cat}, or crossover with probability $1 - P_{\text{cat}}$.

Microtubule nucleation

We explore three distinct modes of microtubule nucleation: isotropic nucleation, global density-dependent nucleation, and a novel local density-dependent nucleation algorithm. The latter consists of a new computational approach, and we compare its performance against the former two methods, already well-studied in the literature [11, 16, 30, 31]. Regardless of the chosen nucleation mode, we assume that nucleation complex availability and behaviour are constant over time. The local density-dependent nucleation algorithm incorporates the following experimental observations: 1) nucleation primarily occurs from the lattice of existing microtubules [15,23,29], 2) with a distribution of relative nucleation angles based on [23], and 3) observations of sparse, oryzalin treated, arrays show that nucleation complexes can appear in empty parts of the array, but have a higher nucleation efficiency after association with a microtubule [12, 15].

Isotropic. In the case of isotropic nucleation, new microtubules are nucleated at a rate r_n. The location and orientation are randomly selected with uniform probability. We hereafter refer to this nucleation mode as ISO.

Global density-dependence. In the global density-dependent nucleation (GDD) case, which was developed in [16], nucleation can be either microtubule-based or background unbound nucleation. Given the total density of tubulin ρ used by microtubules, the rate at which microtubule-based nucleation occurs is

$$r_{n,\text{MT-based}} = r_n \frac{\rho}{\rho + \rho_{1/2}}, \tag{1}$$

where $\rho_{1/2}$ is an equilibrium constant determining the density at which half of the nucleations are microtubule-based [17]. Consequently, isotropic background nucleation occurs at a rate $r_{n,\text{unbound}} = (r_n - r_{n,\text{MT-based}})$. This approach aligns with observations, ensuring that initial nucleations in the microtubule-free membrane are unbound, while a small fraction of unbound nucleations occurs even

at higher densities. In our simulations, the locations of microtubule-based nucleation events are uniformly distributed along the length of all available microtubules.

We modelled the angular distribution of microtubule-based nucleations as proposed by Deinum et al. [16]. Their nucleation mode includes three components: forward (towards the plus-end of the parent microtubule) with probability f_{forward}, backward (towards the minus-end of the parent microtubule) with probability f_{backward}, and the remaining probability sideways, split between left (f_{left}) and right (f_{right}). The sideways angles are modelled proportional to the relative partial surface area from a focal point of an ellipse with eccentricity ϵ, with its main axis oriented with branching angle θ_b relative to the parent model. Parameters ϵ and θ_b are based on the data by Chan and Lloyd [23]. The full nucleation distribution function, denoted as $\nu(\theta)$, where θ is the angle between the direction of the parent and the daughter microtubules, combines these components:

$$\begin{aligned}\nu(\theta) = {} & f_{\text{forward}}\delta(\theta) + f_{\text{backward}}\delta(\theta-\pi) \\ & + \frac{(1-\epsilon^2)^{\frac{3}{2}}}{2\pi}\left[f_{\text{left}}\left(\frac{1}{1-\epsilon\cos(\theta-\theta_b)}\right)^2 + f_{\text{right}}\left(\frac{1}{1-\epsilon\cos(\theta+\theta_b)}\right)^2\right],\end{aligned} \tag{2}$$

where δ is the Dirac δ-distribution.

Local density-dependence. New nucleation complexes appear at the membrane at rate r_{ins} following the observation of nucleation complexes freely diffusing at the membrane [12]. These complexes are virtually placed at a random position $\mathbf{x}_0$ within the simulation domain. For convenience, and without loss of generality, we set $\mathbf{x}_0 = (0,0)$ in the remainder of this section. To define a region for nucleation, we consider a circle with a radius R centered at $\mathbf{x}_0$, which we call the nucleation area. Within this area, we draw N radii, each referred to as a meta-trajectory. The first meta-trajectory is drawn at a random angle $\theta_1 \in [0, 2\pi)$ in the simulation domain, while subsequent meta-trajectories have angles $\theta_i = \theta_{i-1} + 2\pi/N$, see Figure 2A and B. A meta-trajectory labelled by i may either intersect the lattice of a microtubule at a distance r_i from the centre or reach the boundary of the nucleation area, with r_i being equal to the radius R in the latter case. When a meta-trajectory intersects a microtubule lattice, it stops there (Figure 2B). We approximate the diffusion process by assuming that the nucleation complex can either reach these intersections by diffusion or diffuse away from the nucleation area. In our analysis, we set $N = 6$ to reasonably represent the possible directions of diffusion of nucleation complexes.

In general, following the appearance of a nucleation complex at the membrane, three outcomes are possible: (i) the nucleation complex dissociates, (ii) an unbound nucleation occurs, (iii) or the complex reaches the lattice of a microtubule. In the latter case, after reaching a microtubule lattice, the complex may either result in a microtubule-based nucleation or dissociate. The probability that a nucleation complex dissociates is different depending on whether such a complex was freely diffusing or attached to a microtubule lattice. In the former case, the probability of dissociation is 98%, in the latter 76% [12, 15]. Ideally, the nucleation process should be modelled as a two-stage mechanism. Nonetheless, considering the limitation that experimental data are predominantly available for dense arrays and that the rates and probabilities of dissociation are determinable only *a posteriori* [15], i.e., depending on whether a complex has reached a lattice or not, we adopt a pragmatic approach. Initially, we determine the likelihood of a complex reaching a microtubule lattice. Should this happen, within our algorithm, we schedule a microtubule-based nucleation event. If the complex does not reach a microtubule lattice, we then schedule an unbound nucleation.

Subsequently, we reject scheduled nucleation events, applying the relevant rejection probabilities to ensure our model aligns with observed experimental behaviours.

Whether a nucleation complex reaches a microtubule lattice depends on a diffusion process. Indeed, it reaches a lattice if the time it takes to to do so from the moment of the appearance at the plasma membrane is shorter than the waiting time between appearance and unbound nucleation. If the time exceeds this threshold, the result is an unbound nucleation, provided that the potential nucleation is not rejected. We consider this time as deterministic and derive it from the mean squared displacement of a diffusive particle in two dimensions:

$$\tau_i = \frac{d_i^2}{4D}. \tag{3}$$

The waiting time from appearance to unbound nucleation is modeled as exponentially distributed, with an unbound nucleation rate denoted as r_u. Consequently, the probability p that a microtubule reaches the lattice intersected by the meta-trajectory i before unbound nucleation is given by:

$$p(d_i) = \int_{\tau_i}^{\infty} \mathrm{d}t\, r_u e^{-r_u t} = e^{-r_u \frac{d_i^2}{4D}}. \tag{4}$$

Hence, $0.24p(d_i)$ represents the likelihood of a microtubule-based nucleation, given that meta-trajectory i was chosen. Accordingly, $0.02\,(1 - p(d_i))$ is the probability of unbound nucleation given that meta-trajectory i was chosen. In our simulations, we used a maximum meta-trajectory length of $R = 1.5\mu$m because, given our choice of parameters values (Table 1), the probability $p(R)$ of a nucleation complex intersecting with a microtubule lattice prior to nucleation becomes negligible beyond this length. Based on this, the probability of microtubule-based nucleation after a nucleation complex appear at the membrane is

$$p_{\text{MT-based}} = \frac{0.24}{N} \sum_j p(r_j), \tag{5}$$

where the sum over j only runs over meta-trajectories that intersect a microtubule, while the probability of unbound nucleation is $0.02(1 - p_{\text{MT-based}})$, see Figure 2C. We refer to this nucleation mode as local density-dependent (LDD). Note that, for computational efficiency, one could equivalently use $r'_{\text{ins}} = r_{\text{ins}}/0.24$ and accept all possible bound nucleations and possible unbound nucleations with probability $0.083 = 0.02/0.24$.

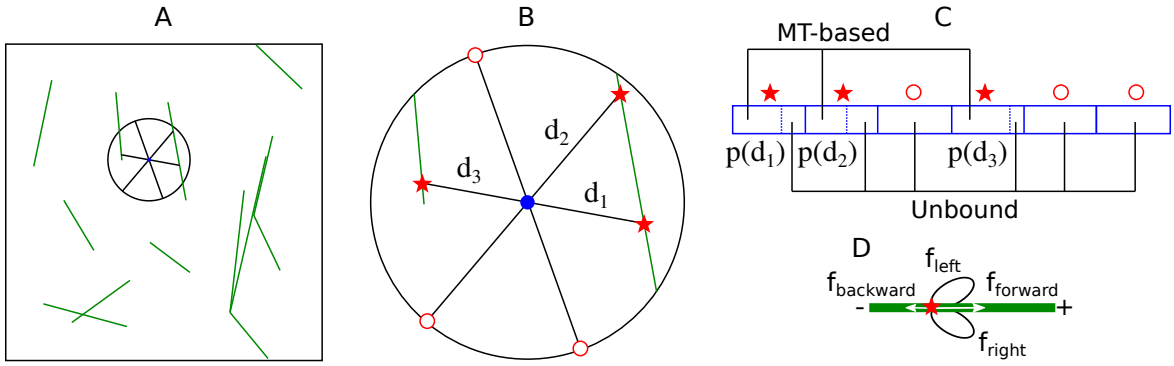

Figure 2: Schematic of the LDD nucleation algorithm. (A) The position in the simulation domain where a nucleation complex appears is selected randomly, with uniform distribution. (B) Such a position, represented by the blue circle, is the centre of the nucleation area (the area included in the black circumference). N meta-trajectories are drawn equidistant from one another and with random orientation. Meta-trajectories are drawn up until the closer between the boundary of the nucleation area or the lattice of an intersecting microtubule. (C) Whether the resulting nucleation is microtubule-based or unbound and, in the former case, the parent microtubule and the nucleation location, is decided stochastically with probability $0.24p(r_i)$ weighted over the length of meta-trajectories, according to Equation (4). (D) In a microtubule-based nucleation, the angles follow [16]: a newly-nucleated microtubule initially grows along the parent microtubule with probability f_{forward}, in the opposite direction with probability f_{backward}, or branches to either side with probability $f_{\text{left/right}}$. The branching angle is determined according to a distribution that closely matches the data in [23].

Degree of alignment and orientation of the array

To assess the alignment of microtubules in a planar system, we use a nematic order parameter S_2 that accounts for the contribution of individual microtubule segments proportionally weighted on their length [16]. For planar geometries, S_2 is defined by

$$S_2 = \sqrt{\langle\langle \cos 2\theta \rangle\rangle^2 + \langle\langle \sin 2\theta \rangle\rangle^2}, \tag{6}$$

where the double brackets denote a length-weighted average over all microtubule segments. S_2 has a value of 0 for an isotropic system and a value of 1 for a system where microtubules are perfectly aligned. For non-planar geometries, we use the order parameter $R_2 \in [0, 1]$ which extends the definition of nematic order parameter to surfaces in the 3D space as defined in [11]. We couple the alignment order parameter S_2 with the overall array orientation Θ_2:

$$\Theta_2 = \arctan\left(\frac{\langle\langle \sin 2\theta \rangle\rangle}{\langle\langle \cos 2\theta \rangle\rangle + S_2}\right). \tag{7}$$

Similarly, for non planar geometries like a capped cylinder, it is possible to extend the definition of Θ_2 to surfaces in the 3D space [11].

Navigating parameter space with control parameter G

The driver of spontaneous alignment in the cortical array is the occurrence of sufficient interactions within the average microtubule length. This is quantified by a single control parameter G [8, 9], which is the ratio of two length scales: an interaction length scale (left factor) and the average length of non-interacting microtubules (right factor). We use a version of G adjusted for minus end treadmilling [16]:

$$G = \left(\frac{2(v^+ - v^{\mathrm{tm}})^2 (v^- + v^{\mathrm{tm}})}{r_n v^+ (v^+ + v^-)} \right)^{1/3} \left(\frac{r_r}{v^- + v^{\mathrm{tm}}} - \frac{r_c}{v^+ - v^{\mathrm{tm}}} \right). \tag{8}$$

Note that we restrict ourselves to $G < 0$, i.e., when microtubules are in the so-called bounded-growth regime, where they have a finite life span and finite intrinsic length. In this case, spontaneous alignment occurs if $G > G^*$, some threshold that depends on the details of microtubule-microtubule interactions. In graphs where we vary G, we use the notation G_c to indicate that G is varied via r_c.

For ISO and GDD nucleation modes, the nucleation rate r_n is an explicit simulation parameter. For LDD nucleation, however, r_n results from the interplay between the rate at which nucleation complexes appear at the membrane r_{ins} and rejection of nucleations, which in turn depends on the density and distribution of the microtubules. Therefore, we calculate the effective nucleation rate to be used for G in Equation (8) as

$$r_n = \frac{n_c(T)}{TA}, \tag{9}$$

where $n_c(T)$ is the number of nucleation events occurred after time T, and A is the area of the simulation domain. In principle, n_c might be non-linear in T, making our proposed computation of r_n overly-simplistic. However, our test showed that $n_c(T)$ is approximately linear in T, for $T < 3 \times 10^4$ seconds, see Figure S1.

Results

In this section, we used default parameter values listed in Table 1. The default simulation domain in a square grid with periodic boundary conditions and size $L = 40\mu$m. We tuned the value of the parameter G by varying the catastrophe rate r_c. The above, if not otherwise indicated, should be considered our default parameter values and the basis of our analysis.

LDD nucleation results in homogeneous aligned arrays

We first studied the self-organisation of the cortical microtubule array in two-dimensional rectangles with periodic boundary conditions, and different sizes: $L = 80\mu$m and $H = 80\mu$m, $L = 40\mu$m and $H = 40\mu$m, $L = 20\mu$m and $H = 20\mu$m, $L = 20\mu$m and $H = 40\mu$m, $L = 20\mu$m and $H = 80\mu$m. More specifically, we compared snapshots of the cortical array at $T = 3 \times 10^4$ seconds in the aligned regime, analysing arrays obtained through LDD, GDD, and ISO nucleation modes. The threshold value of the control parameter G, at which the array can be considered aligned, varies according to the size and aspect ratio of the simulation domain. This threshold was determined by measuring the degree of alignment S_2 averaged over 100 simulation runs, across the five distinct simulation domains as a function of G (Figure S2).

Figure 3 shows snapshots of aligned arrays for each studied geometry and nucleation mode. The degree of alignment S_2 of the snapshots provided accurately reflects the average degree of alignment in relation to the control parameter G (see Figure S2). The visual representation shows that simulations using the LDD mode resulted in homogeneous arrays across various geometries, akin to those obtained with the ISO mode. Partial inhomogeneity, as observed in LDD (Figure 3D), was transient, as shown in Figure S3A. Conversely, in the GDD mode, homogeneity was hardly restored or even achieved at all, as illustrated in Figure S3B. The striking difference between LDD and GDD can be attributed to the appearance of new nucleation complexes at random location throughout the simulation domain in LDD. This, in principle, can ensure that newly-nucleated microtubules are introduced more uniformly, leading to a roughly even distribution across various regions of the simulation domain and in the different bundles. In contrast, the positive feedback mechanism in GDD primarily directed new microtubules to already densely populated bundles. It could only nucleate new microtubules to sparsely populated areas through background unbound nucleation, which occurred rarely at high density, according to Equation (1).

Moreover, we observed in Figure 3A that, while homogeneity in the LDD and ISO modes was similar, there were significant differences in the level of alignment. In the former case, the alignment was higher, with $S_2 = 0.93$, compared to $S_2 = 0.84$ in ISO, see also Figure S2. This suggests that, even for large geometries, LDD could sustain an alignment of the array, likely caused by strong orientational correlations. In contrast, ISO exhibited different local ordering emerging from the simulation, partially hindering the alignment of the array.

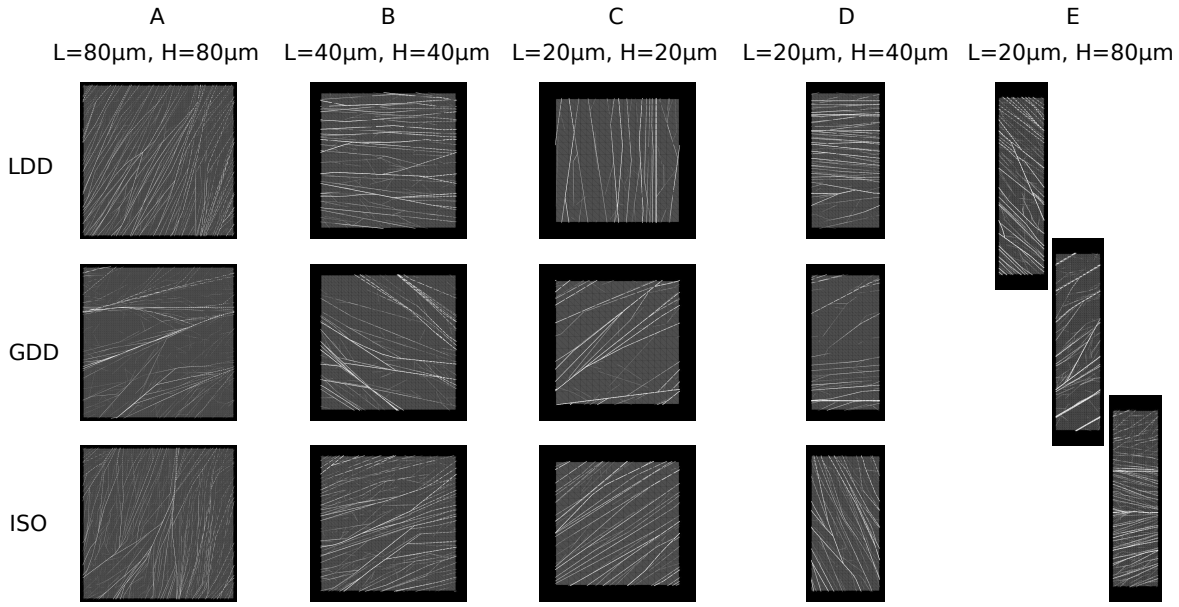

Figure 3: Snapshot of the simulation domain at $T = 3 \times 10^4$ seconds with different sizes of the domain with periodic boundary conditions. The different domain sizes are not in scale with each other for visibility.
(A) LDD: $S_2 = 0.93$, $G = -0.19$. GDD: $S_2 = 0.85$ $G = -0.27$. ISO: $S_2 = 0.84$, $G = -0.14$.
(B) LDD: $S_2 = 0.96$, $G = -0.19$. GDD: $S_2 = 0.89$, $G = -0.23$. ISO: $S_2 = 0.90$, $G = -0.14$.
(C) LDD: $S_2 = 0.97$, $G = -0.18$. GDD: $S_2 = 0.88$, $G = -0.14$, ISO: $S_2 = 0.97$, $G = -0.12$.
(D) LDD: $S_2 = 0.97$, $G = -0.19$. GDD: $S_2 = 0.95$, $G = -0.25$. ISO: $S_2 = 0.95$, $G = -0.14$.
(E) LDD: $S_2 = 0.91$, $G = -0.20$. GDD: $S_2 = 0.89$, $G = -0.27$. ISO: $S_2 = 0.83$, $G = -0.16$.

LDD nucleation increases the regime of spontaneous alignment

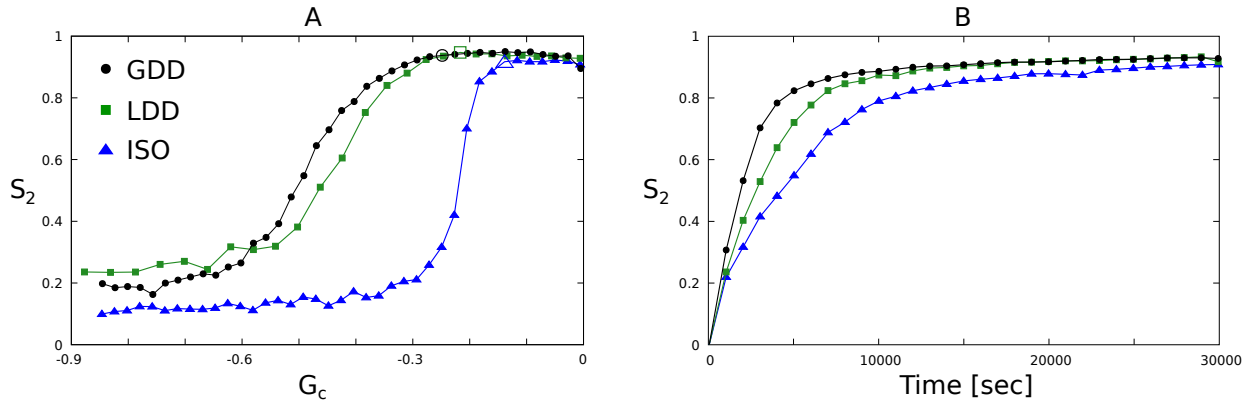

Figure 4: Order regime for LDD, GDD, and ISO nucleation modes in a squared geometry with sizes $L = 40\mu$m and $H = 40\mu$m. (A) Order parameter S_2 as function of the control parameter G at $T = 3 \times 10^4$ sec, averaged over 100 independent simulation runs. Data points marked as larger, empty circle, square, or triangle correspond to the parameter values used for panel (B). (B) Order parameter S_2 as function of the simulation time. Results are averaged over 100 independent runs for selected values of G (data points marked in red in panel (A)) in the order regime. Error bars of (A) can be found in Figure S4.

We computed the order parameter S_2 as a function of the control parameter G at $T = 3 \times 10^4$ seconds averaged over 100 simulations for LDD, GDD, and ISO nucleation modes. Figure 4A shows that, compared to ISO, LDD expanded the range of values of G such that the array was well aligned in a preferred direction, with a similar behaviour for the $S_2(G)$ curve to GDD. More specifically, the aligned regime could be achieved for roughly the same G values as in the GDD case. For intermediate values of G, although the behaviour was more comparable to GDD that it was to ISO, LDD produces a less aligned array, likely consequence of the higher number of background nucleation compared to what happened for higher G values, i.e., when more collisions occurred. Figure S2 shows that, in the LDD and ISO cases, increasing the size of the simulation domain had the potential to lower the value of the order parameter S_2 due to the creation of local ordering (see also Figure 3A). In the GDD case, this effect was less pronounced, likely due to the high probability of nucleation of new microtubules from extant microtubules in already highly populated bundles. This did not occur in ISO and LDD.

In the aligned regime, due to microtubule-based nucleation being more likely than unbound nucleation, the alignment of the array occurred at a faster pace than in the ISO case, though not as fast as in the GDD, see Figure 4B. Again, the positive feedback loop attracting the nucleation of new microtubules in densely populated bundles significantly accelerated alignment, since newly-nucleated microtubules are more likely to initially grow in a direction similar to that of their parent microtubules, as theoretically shown by Foteinopoulos and Mulder [17]. This inclination of new microtubules towards an already established preferred direction of alignment, while present in the LDD scenario, was substantially less pronounced than in GDD.

LDD is a bias-free algorithm for microtubule nucleation

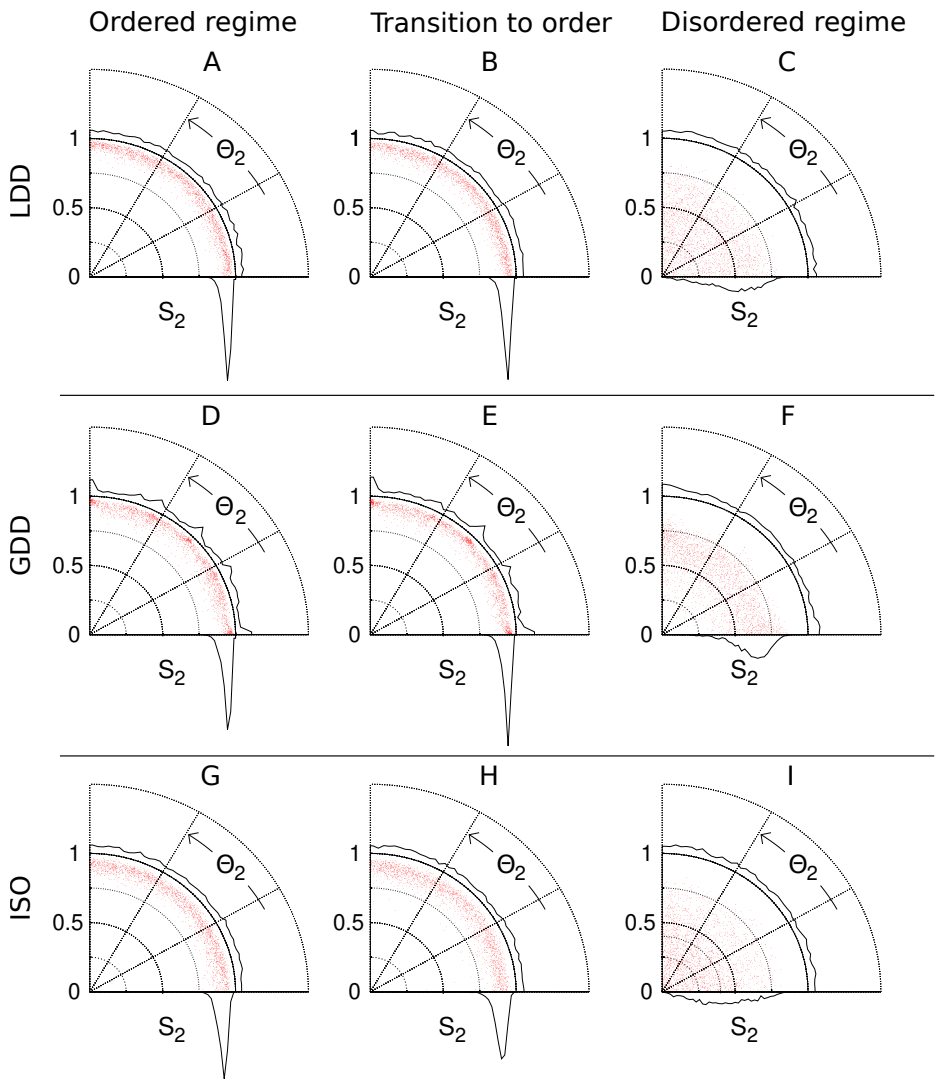

Figure 5: Distribution of S_2 and Θ_2 for three different regimes. Each panel contains the result in terms of alignment S_2 and orientation Θ_2 of 2000 independent runa at $T = 3 \times 10^4$ sec. A point located along the horizontal axis represents a perfectly transverse array orientation, while a point on the vertical axis represents a perfectly longitudinal orientation. The distance of the point from the origin indicates the strength of the alignment, with greater distances indicating a higher degree of alignment. The data points are collected to generate histograms for the distribution of S_2 (horizontal axis) and Θ_2 (vertical axis). G values: (A) $G = -0.22$, (B) $G = -0.25$, (C) $G = -0.42$, (D) $G = -0.23$, (E) $G = -0.25$, (F) $G = -0.54$, (G) $G = -0.16$, (H) $G = -0.18$, (I) $G = -0.25$. Panels (A), (D), and (G) correspond to the empty markers of Figure 4A.

Figure 5 shows the distribution of both order parameters S_2 and Θ_2 over 2000 simulation runs for LDD (Figure 5A-C), GDD (Figure 5D-F), and ISO (Figure 5G-I), each for three different values of

the parameter G that correspond to aligned array (Figure 5A, D, and G), transition to fully aligned array (Figure 5B, E, and H), and disordered array (Figure 5C, F, and I). As we would expect, in the case of LDD and ISO nucleation, the distribution of Θ_2 after $T = 3 \times 10^4$ sec was uniform for each of the three G values. On the contrary, in the case of GDD nucleation, computational artefacts arose. Indeed, Figure 5D shows five preferential alignments for an ordered array: $\Theta_2 = 0$, $\Theta_2 = \pi/8$, $\Theta_2 = \pi/4$, $\Theta_2 = 3\pi/8$, and $\Theta_2 = \pi/2$, see Figure 5D. The $\Theta_2 = 0$ and $\Theta_2 = \pi/2$ alignments are due the presence of bundles that wrapped around themselves along the shortest possible path. This effect, which should be in principle visible for LDD and ISO too, was only recorded in the GDD case due to the inhomogeneity problem, i.e., the presence of few highly populated and, therefore, very long, bundles. The remaining three preferred orientations at $\Theta_2 = \pi/8$, $\Theta_2 = \pi/4$, $\Theta_2 = 3\pi/8$ are a computational artefact due to the subdivision of the simulation domain in small square grid cells, with the consequence of more likely selecting as parent microtubules those that were aligned along the (anti-)diagonal of such square grids, or even the combination of two adjacent square grids. For slightly lower interaction strength, i.e., lower G (Figure 5E), only $\Theta_2 = 0$, $\Theta_2 = \pi/4$, and $\Theta_2 = \pi/2$ preferred orientation survived. Though this bias was relatively small, it could be relevant when one wants to study the response of the array as a whole to small directional cues.

Note that, in the disordered state, LDD and ISO lead to similar distributions for both S_2 and Θ_2, where the former tended to be relatively flat and the latter was very uniform, especially when compared to the GDD scenario. In GDD, the preferred orientations of $\Theta_2 = 0$ and $\Theta_2 = \pi/2$ were somewhat preserved, and S_2 exhibits peaks in the distribution at average values, as shown in Figure 5C, F, and I. This phenomenon could be attributed to LDD primarily involving unbound nucleation at low G values, at which point the microtubule density was average. In contrast, GDD continued to support a significant amount of microtubule-based nucleation, which had the capability to form densely packed bundles.

Local and global density-dependence emerge from LDD nucleation

To verify that our proposed LDD nucleation mode exhibits density-dependence in the probability of microtubule-based nucleation, we computed the fraction of such nucleation events relative to the total number of nucleation events as a function of the density of microtubule length per unit of area. This assessment was conducted at both local and global scales. The global microtubule density was computed using the formula $\rho = \sum_i l_i/A$, where l_i represents the length of the i-th microtubule, the summation runs over all microtubules, and A denotes the area of the simulation domain. Instead, the local tubulin density was determined by the formula $\rho = \sum_{i,j} l_{i_j} / \sum_j A_j$. In this expression, l_{i_j} represents the length of the segment of the i-th microtubule within region j with area A_j, and j runs over all regions touched by the metatrajectories drawn from the appearance location of a nucleation complex, as shown by the schematic in Figure 6A.

Figure 6 shows that density-dependence of microtubule-based nucleation naturally emerged from LDD mode without being imposed by Equation (1) as in the GDD case. This density-dependence behaviour was maintained across local and global scale. We fitted the data from our simulations by superimposing the fitting function $\rho/(\rho + a)$ and we obtained $a = 0.19 \pm 0.01$ for the local microtubule density (Figure 6A), and $a = 0.18 \pm 0.01$ for the global microtubule density (Figure 6B).

Note that, at high microtubule density ($\rho \simeq 5\mu\text{m}^{-1}$), the frequency of occurrence of microtubule-based nucleation remained below 1, specifically around 0.95 for high local density (as shown in Figure 6A) and 0.9 for high global density (Figure 6B). These frequencies were lower than the experimentally measured value of approximately 0.98 by Nakamura et al. [15]. This discrepancy

could arise from the fact that, in our simulations, we did not consider that nucleation complexes appear at the membrane preferentially in the vicinity of microtubule lattices [12, 13], which would lead to a higher likelihood of microtubule-based nucleation. Consequently, our algorithm slightly underestimated the frequency of occurrence of microtubule-based nucleation events.

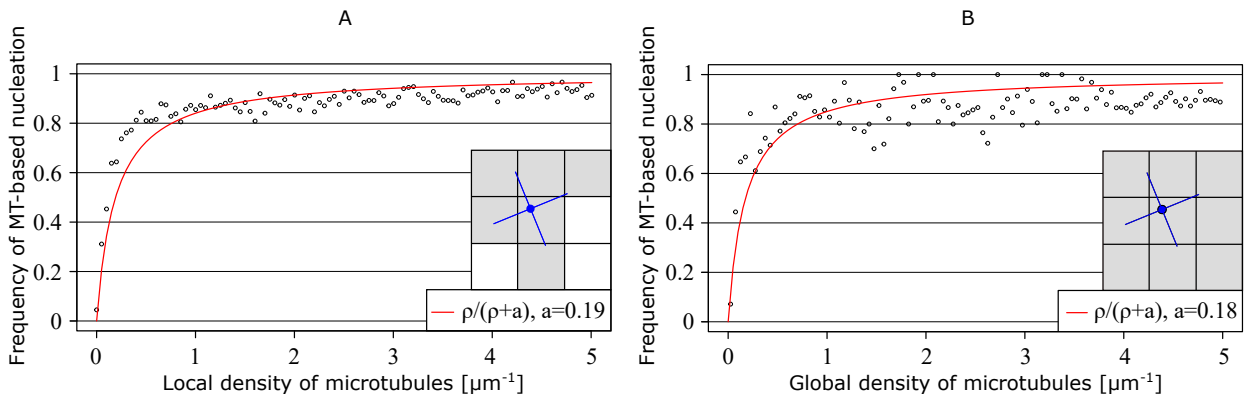

Figure 6: Frequency of microtubule-based nucleation as a function of (A) local and (B) global density of microtubules for a simulation run. In this simulation, $r_c = 0.0025$ sec^{-1}.

Geometrical effects on the orientation of alignment

We tested how our algorithm influenced array alignments within more complex and realistic cellular geometries by running simulations on two cylindrical domains. These domains maintained a constant height-to-diameter ratio while varying the overall dimensions of the cylinders. We incorporated two distinct directional biases independently: a global bias, represented by a 8% increase in the catastrophe rate at the cylinder caps, and a local bias, with a maximum 8% directional enhancement in the rescue rate for individual microtubules. Mathematically, the adjustment in the rescue rate is expressed as:

$$r_{r,\text{extra}} = \frac{b_{\max}}{2}\left[1 + \cos\left(2(\theta - \theta_r)\right)\right], \tag{10}$$

where θ denotes the shrinkage direction of the microtubule plus end, θ_r represents the angle at which the rescue rate is maximum, and $b_{\max} = 0.08$ is the maximal increase factor when $\theta = \theta_r$.

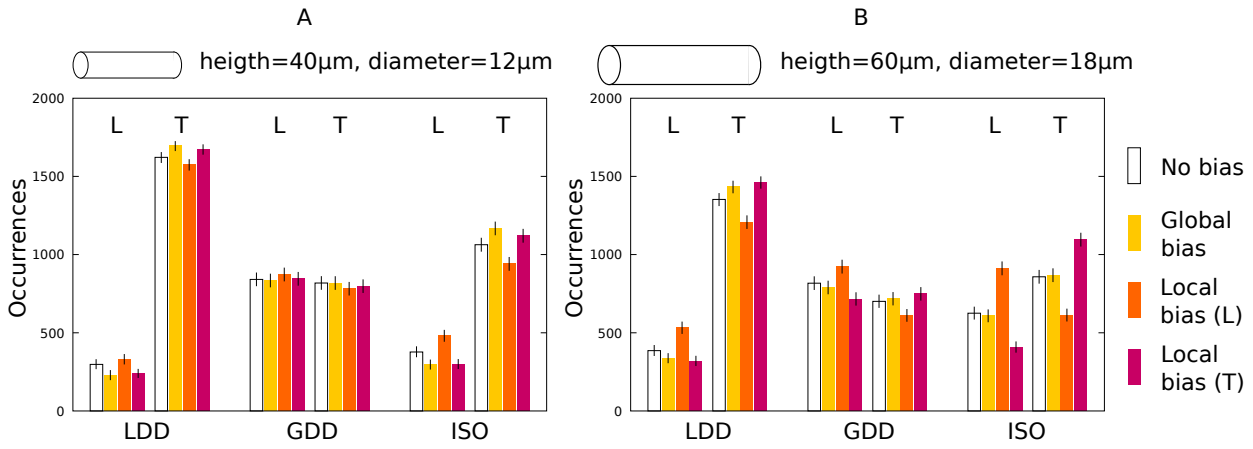

Figure 7: Number of aligned arrays at $T = 3 \times 10^4$ sec with a transverse (T; when $-10° < \Theta_2 < 10°$), or longitudinal (L; when $80° < \Theta_2 < 100°$) orientation, with or without directional biases: 8% increase in catastrophe rate at the cylinder caps for the global bias, and 8% increase in maximum rescue rate according to Equation (10) for the local bias. The simulation domain is a cylinder of (A) 40μm length and 12μm diameter, and (B) 60μm length and 18μm diameter. Error bars represent 95% confidence interval according to a binomial model (computed using the binom.test function in R statistical package version 3.6.3).

Figure 7 shows the frequency of alignment in both longitudinal ($80° < \Theta_2 < 100°$) and transverse ($-10° < \Theta_2 < 10°$) orientations across 2000 simulation runs for the three nucleation modes and different orientational biases. The LDD method exhibited a pronounced preference for transverse alignment over longitudinal. This preference could be explained by the formation of "bracelets" of microtubule bundles that wrapped around themselves, as shown in Figure S5B. In a smaller cylindrical domain, more than 75% of the simulations resulted in a transverse orientation of the microtubule arrays. This outcome was consistent regardless of the incorporation of global or local biases (Figure 7A). For larger simulation domains (Figure 7B), a strong inclination towards transverse orientation remained evident. However, in the latter case, slight directional biases favouring longitudinal orientation slightly increased the instances of longitudinal array formations, though less frequently than transverse arrays. The observed phenomenon likely stemmed from the extended trajectories required by transverse bundles to complete their self-wrapping process, which marginally promoted the emergence of local ordering in other directions than transverse

Figure 7A also shows that in smaller simulation domains, the GDD nucleation mode did not exhibit a preference for either orientation, with minor directional signals (both global and local) having little impact on establishing a preferred alignment. This observation is related to intense competition among initially forming aligned arrays, which predominantly consisted of one or two densely populated bundles, as shown in Figure S5A. Surprisingly, in larger cylindrical domains, we observed a slight predisposition towards longitudinal orientation over transverse orientation. This can be understood by noting that slight deviations from a transverse orientation can be detrimental for the stability of densely populated bundles. When these bundles are excessively long, i.e., when they reach the cap of the cylinder and return back with mirrored orientation, they risk colliding with themselves, with individual microtubules in the bundle undergoing induced catastrophes, potentially causing initial transverse bundles to be outcompeted by initially longitudinal bundles (Figure S5A).

These longitudinal bundles, in contrast, benefit from the topology of the simulation domain, offering them greater stability against minor deviations relative to the longitudinal direction. Similar to the LDD scenario, both global and local cues appeared to have a more pronounced influence in determining orientation in larger domains compared to smaller ones.

When nucleation occurred isotropically, the addition of directional biases had a more significant effect on the preferred orientation of the cortical array than observed with the LDD and GDD modes. This effect was particularly evident in larger simulation domains, where a local directional bias could effectively determine the preferred orientation of the cortical array, as shown in Figure 7B and in line with previous results [21].

Discussion

In this work, we have developed a novel, computational time efficient nucleation algorithm for realistic microtubule bound nucleation that does not suffer from the inhomogeneity problem that haunted the field for over a decade [12, 13, 16, 30]. We showed that different nucleation algorithms can have great impact on the overall behaviour of the cortical array. In particular, microtubule-based nucleation with local microtubule density-dependence extended the length and life time of microtubule bundles, thereby increasing the regime of spontaneous alignment and making the array more sensitive to subtle orientational cues from the cell's geometry. The ability to simulate this force realistically, opens up the possibility of quantitative comparison of different forces acting on array orientation.

A major open question in the field is how plant cells weigh different cues affecting the orientation of the cortical array. Such cues can be global, i.e., that always require information processing throughout the whole array, and local, i.e., that can be sensed (almost) everywhere in the cortex with similar intensity. The most prominent global cue derives directly from the cell geometry itself, as only a limited set of array orientations minimizes conflicts with itself [5, 19]. Cues like penalties for crossing (sharp) edges [5, 37] or cell faces with less favourable conditions can more selectively determine which orientations are realized [5, 19, 38]. In terms of information processing, these act as global cues.

In contrast, the co-alignment of microtubules with patterns of mechanical stress in the cell wall that seems to dominate in certain systems [20, 27, 39–42], is typically assumed to happen via local cues, e.g., implemented as a slight bias in the microtubule growth direction towards the direction of (predicted) maximum wall stress [21], or increased growth propensity for co-aligned microtubules via the modulation of microtubule dynamics in simulation studies [38, 43]. The exact mechanism behind this observation remains elusive, but depends on katanin [41, 42]. This microtubule severing enzyme [44, 45] has a profound influence on alignment of the cortical array and is critically important for array reorientation in response to various internal or external cues [33, 41, 42, 46, 47]. Another local cue is the tendency of some microtubules to slowly reorient such that they minimize their curvature either globally or over a small region, e.g., favouring longitudinal orientation on an infinite cylinder [48–50]. As these results all stem from theoretical work on non-interacting microtubules, the practical relevance of this tendency still is subject to debate.

The question which cues are most important in orienting the microtubule array, therefore, also depends on the relative impact of local and global cues. The balance between local and global cues depends on the intrinsic (non-interacting) length of individual microtubules relative to the cell's dimensions, as this length scale affects how far and how easily the information of global cues

propagates throughout the array [18], also, compare figure 7A and B. This balance can be further tuned towards local cues by reducing the microtubule persistence length [24,38,51] or towards global cues by increasing the persistence of microtubule bundles. Microtubule-based nucleation, which has a substantial fraction of nucleations parallel or anti-parallel to the parent microtubule [23], can extend microtubule bundles and increase their life span [16]. As such, microtubule-based nucleation increases the relative impact of global orienting cues (compare LDD and isotropic nucleation in Figure 7). Such considerations emphasise the importance of microtubule simulations with a sufficient degree of realism in different aspects.

Here, our work plays a very import role. The algorithm we present allows for the efficient simulation of microtubule-based nucleation, whilst avoiding the problem of artificial inhomogeneity. Various experimental have shown that the responsiveness of array orientation to different cues critically depends on microtubule severing enzyme katanin [22, 39, 41, 42, 46, 52, 53]. With our new algorithm, the simulation platform CorticalSim now is equipped with both realistic katanin severing [33], semiflexible microtubules [24], and advanced microtubule-based nucleation.

Besides the competition between different cues affecting array orientation, our algorithm has diverse other application areas. We name two additional examples. 1) The control of patterned secondary cell wall deposition, e.g., in xylem elements [12, 13, 24]. These regular patterns cannot be formed if the inhomogeneity problem appears, but timely separation of the array into future gaps and dense regions does require the positive feedback resulting from microtubule-based nucleation [13, 24]. 2) Consistent organ twisting and/or bending through the formation of helical arrays with predictable handedness [54,55], as observed, for example, in the *spiral* [56,57] and *lefty* mutants [58,59], in various mutants with point mutations in tubulin subunits that affect microtubule stability [60, 61], and following treatment with various drugs that affect microtubule stability [56,62]. What remains unclear is how changes in microtubule dynamics couple to chiral biases in the structure of microtubules, microtubule associated protein and/or the cell wall [63–65], and whether the array would adopt a fixed tilted orientation in isolated cells, or the observed array orientation would arise from a balance between competing rotating and counteracting forces, including tensile forces [66, 67], on the array. Again, we predict that the bundle elongating effect of microtubule-based nucleation will substantially impact such a balance. Another important question for organ twisting is how reliable array orientation at the level of single, isolated cells would need to be for a consistent, predictable outcome at the organ level, mediated through the mechanical coupling of cells and cell files [67]. Obviously, investigating this question would require integrating explicit microtubule simulations in a multi-level modelling approach.

Our computational advances enable the *in silico* investigation of the plant cortical array with unprecedented realism in a fast simulation environment. Compared to previous nucleation algorithms, this algorithm does not introduce artifacts related to the inhomogeneity problem as GDD-like algorithms [13, 16, 30], resulting in simulated cells that would have serious problems with cell wall integrity, but does offer the saturating, positive feedback on local microtubule density that is missing with isotropic nucleation, which supports patterning of the cortical array [12, 24] and increases the sensitivity to global cues. This advance supports a quantitative level of investigation that allows to distinguish between competing biophysical mechanisms. As illustrated by the examples above, there are many open questions that can be addressed with help of our new algorithm.

References

[1] Ehrhardt DW, Shaw SL. Microtubule dynamics and organization in the plant cortical array. Annual Review of Plant Biology. 2006;57:859–75.

[2] Sablowski R. Coordination of plant cell growth and division: collective control or mutual agreement? Current Opinion in Plant Biology. 2016;34:54–60.

[3] Wasteneys GO. Microtubule organization in the green kingdom: chaos or self-order? Journal of Cell Science. 2002;115:1345.

[4] Chan J, Coen E. Interaction between autonomous and microtubule guidance systems controls cellulose synthase trajectories. Current Biology. 2020;30(5):941–947.

[5] Chakrabortty B, Willemsen V, de Zeeuw T, Liao CY, Weijers D, Mulder B, et al. A plausible microtubule-based mechanism for cell division orientation in plant embryogenesis. Current Biology. 2018;28(19):3031–3043.

[6] Gutierrez R, Lindeboom JJ, Paredez AR, Emons AM, Ehrhardt DW. Arabidopsis cortical microtubules position cellulose synthase delivery to the plasma membrane and interact with cellulose synthase trafficking compartments. Nature Cell Biology. 2009;11(7):797–806.

[7] Paredez AR, Somerville CR, Ehrhardt DW. Visualization of Cellulose Synthase Demonstrates Functional Association with Microtubules. Science. 2006;312(5779):1491–1495.

[8] Tindemans SH, Hawkins RJ, Mulder BM. Survival of the aligned: ordering of the plant cortical microtubule array. Phys Rev Lett. 2010;104(5):058103.

[9] Deinum EE, Mulder BM. Modelling the role of microtubules in plant cell morphology. Curr Opin Plant Biol. 2013;16(6):688–692.

[10] Dixit R, Cyr R. Encounters between Dynamic Cortical Microtubules Promote Ordering of the Cortical Array through Angle-Dependent Modifications of Microtubule Behavior. The Plant Cell. 2004;16(12):3274–3284.

[11] Tindemans SH, Deinum EE, Lindeboom JJ, Mulder B. Efficient event-driven simulations shed new light on microtubule organisation in the plant cortical array. Frontiers in Physics. 2014;2(19):9.

[12] Jacobs B, Schneider R, Molenaar J, Filion L, Deinum EE. Microtubule nucleation complex behavior is critical for cortical array homogeneity *and* xylem wall patterning. Proceedings of the National Academy of Sciences. 2022;119(50):e2203900119.

[13] Schneider R, Klooster Kv, Picard KL, van der Gucht J, Demura T, Janson M, et al. Long-term single-cell imaging and simulations of microtubules reveal principles behind wall patterning during proto-xylem development. Nature communications. 2021;12(1):1–12.

[14] Sambade A, Pratap A, Buschmann H, Morris RJ, Lloyd C. The influence of light on microtubule dynamics and alignment in the Arabidopsis hypocotyl. Plant Cell. 2012;24(1):192–201.

[15] Nakamura M, Ehrhardt DW, Hashimoti T. Microtubule and katanin-dependent dynamics of microtubule nucleation complexes in the acentrosomal Arabidopsis cortical array. Nature Cell Biology. 2010;12(11):1064–70.

[16] Deinum EE, Tindemans SH, Mulder BM. Taking directions: the role of microtubule-bound nucleation in the self-organization of the plant cortical array. Phys Biol. 2011;8(5):056002.

[17] Foteinopoulos P, Mulder BM. The effect of anisotropic microtubule-bound nucleations on ordering in the plant cortical array. Bulletin of mathematical biology. 2014;76(11):2907–2922.

[18] Chakrabortty B, Blilou I, Scheres B, Mulder BM. A computational framework for cortical microtubule dynamics in realistically shaped plant cells. PLoS computational biology. 2018;14(2):e1005959.

[19] Deinum EE, Mulder BM. Modelling the Plant Microtubule Cytoskeleton. In: Morris RJ, editor. Mathematical Modelling in Plant Biology. Springer; 2018. p. 53–67.

[20] Hamant O, Heisler MG, Jonsson H, Krupinski P, Uyttewaal M, Bokov P, et al. Developmental patterning by mechanical signals in Arabidopsis. Science. 2008;322(5908):1650–5.

[21] Mirabet V, Krupinski P, Hamant O, Meyerowitz EM, Jönsson H, Boudaoud A. The self-organization of plant microtubules inside the cell volume yields their cortical localization, stable alignment, and sensitivity to external cues. PLoS computational biology. 2018;14(2):e1006011.

[22] Saltini M, Mulder BM. A plausible mechanism for longitudinal lock-in of the plant cortical microtubule array after light-induced reorientation. Quantitative Plant Biology. 2021;2:e9.

[23] Chan J, Sambade A, Calder G, Lloyd C. Arabidopsis Cortical Microtubules Are Initiated along, as Well as Branching from, Existing Microtubules. Plant Cell. 2009;12(8):2298–306.

[24] Jacobs B, Saltini M, Molenaar J, Filion LC, Deinum EE. Protoxylem microtubule patterning requires ROP pattern co-alignment, realistic microtubule-based nucleation, and sufficient microtubule flexibility. bioRxiv. 2024;doi:https://doi.org/10.1101/2024.04.04.588070.

[25] Hawkins T, Mirigian M, Yasar MS, Ross JL. Mechanics of microtubules. Journal of biomechanics. 2010;43(1):23–30.

[26] Durand-Smet P, Spelman TA, Meyerowitz EM, Jönsson H. Cytoskeletal organization in isolated plant cells under geometry control. Proceedings of the National Academy of Sciences. 2020;117(29):17399–17408.

[27] Colin L, Chevallier A, Tsugawa S, Gacon F, Godin C, Viasnoff V, et al. Cortical tension overrides geometrical cues to orient microtubules in confined protoplasts. Proceedings of the National Academy of Sciences. 2020;.

[28] Gomez JM, Chumakova L, Bulgakova NA, Brown NH. Microtubule organization is determined by the shape of epithelial cells. Nature Communication. 2016;7:13172.

[29] Murata T, Sonobe S, Baskin TI, Hyodo S, Hasezawa S, Nagata T, et al. Microtubule-dependent microtubule nucleation based on recruitment of gamma-tubulin in higher plants. Nature Cell Biology. 2005;7(10):961–8.

[30] Allard JF, Wasteneys GO, Cytrynbaum EN. Mechanisms of self-organization of cortical microtubules in plants revealed by computational simulations. Molecular Biology of the Cell. 2010;21(2):278–86.

[31] Eren EC, Dixit R, Gautam N. A 3D Computer Simulation Model Reveals the Mechanisms for Self-Organization of Plant Cortical Microtubules into Oblique Arrays. Mol Biol Cell. 2010;21(15):2674–84.

[32] Motta MR, Nedelec F, Woelken E, Saville H, Jacquerie C, Pastuglia M, et al. The cell cycle controls spindle architecture in Arabidopsis by modulating the augmin pathway. bioRxiv. 2023; p. 2023–11.

[33] Deinum EE, Tindemans SH, Lindeboom JJ, Mulder BM. How selective severing by katanin promotes order in the plant cortical microtubule array. Proceedings of the National Academy of Sciences. 2017;114(27):6942–6947.

[34] Jacobs B. Exploring mechanisms of xylem cell wall patterning with dynamic models. Wageningen University and Research; 2022.

[35] Dogterom M, Leibler S. Physical aspects of the growth and regulation of microtubule structures. Physical Review Letters. 1993;70:1347.

[36] Shaw SL, Kamyar R, Ehrhardt DW. Sustained Microtubule Treadmilling in Arabidopsis Cortical Arrays. Science. 2003;300(5626):1715–1718.

[37] Ambrose C, Allard JF, Cytrynbaum EN, Wasteneys GO. A CLASP-modulated cell edge barrier mechanism drives cell-wide cortical microtubule organization in *Arabidopsis*. Nature Communication. 2011;2:430.

[38] Saltini M, Deinum EE. Microtubule simulations in plant biology: a field coming to maturity. Curr Opin Plant Biol. 2024;doi:10.1016/j.pbi.2024.102596.

[39] Uyttewaal M, Burian A, Alim K, Landrein B, Borowska-Wykret D, Dedieu A, et al. Mechanical stress acts via katanin to amplify differences in growth rate between adjacent cells in *Arabidopsis*. Cell. 2012;149:439.

[40] Louveaux M, Julien JD, Mirabet V, Boudaoud A, Hamant O. Cell division plane orientation based on tensile stress in *Arabidopsis thaliana*. Proceedings of the National Academy of Science. 2016;113:E4294.

[41] Sampathkumar A, Krupinski P, Wightman R, Milani P, Berquand A, Boudaoud A, et al. Subcellular and supracellular mechanical stress prescribes cytoskeleton behavior in Arabidopsis cotyledon pavement cells. Elife. 2014;3:e01967.

[42] Eng RC, Schneider R, Matz TW, Carter R, Ehrhardt DW, Jönsson H, et al. KATANIN and CLASP function at different spatial scales to mediate microtubule response to mechanical stress in Arabidopsis cotyledons. Current Biology. 2021;.

[43] Smithers ET. Using mathematical modelling to understand how plant cell growth is controlled. University of Birmingham; 2022.

[44] Burk DH, Liu B, Zhong R, Morrison WH, Ye ZH. A Katanin-like Protein Regulates Normal Cell Wall Biosynthesis and Cell Elongation. THE PLANT CELL. 2001;13(4):807.

[45] Bichet A, Desnos T, Turner S, Grandjean O, Höfte H. BOTERO1 is required for normal orientation of cortical microtubules and anisotropic cell expansion in Arabidopsis. The Plant Journal. 2001;25(2):137–148.

[46] Lindeboom JJ, Nakamura M, Hibbel A, Shundyak K, Gutierrez R, Ketelaar T, et al. A mechanism for reorientation of cortical microtubule arrays driven by microtubule severing. Science. 2013;342(6163):1245533.

[47] Saltini M, Mulder BM. Critical threshold for microtubule amplification through templated severing. Physical Review E. 2020;101:052405.

[48] Lagomarsino MC, Tanase C, Vos JW, Emons AMC, Mulder BM, Dogterom M. Microtubule Organization in Three-Dimensional Confined Geometries: Evaluating the Role of Elasticity Through a Combined In Vitro and Modeling Approach. Biophysical Journal. 2007;92(3):1046.

[49] Bachmann S, Froese R, Cytrynbaum EN. A buckling instability and its influence on microtubule orientation in plant cells. SIAM Journal on Applied Mathematics. 2019;79(5):2132–2149.

[50] Tian TY, Macdonald CB, Cytrynbaum EN. A stochastic model of cortical microtubule anchoring and mechanics provides regulatory control of microtubule shape. Bulletin of Mathematical Biology. 2023;85(11):1–23.

[51] Sasaki T, Saito K, Inoue D, Serk H, Sugiyama Y, Pesquet E, et al. Confined-microtubule assembly shapes three-dimensional cell wall structures in xylem vessels. Nature Communications. 2023;14(1):6987.

[52] Nakamura M, Lindeboom JJ, Saltini M, Mulder BM, Ehrhardt DW. SPR2 protects minus ends to promote severing and reorientation of plant cortical microtubule arrays. Journal of Cell Biology. 2018;217(3):915–927.

[53] Lindeboom JJ, Nakamura M, Saltini M, Hibbel A, Walia A, Ketelaar T, et al. CLASP stabilization of plus ends created by severing promotes microtubule creation and reorientation. Journal of Cell Biology. 2019;218(1):190–205.

[54] Wada H. Hierarchical helical order in the twisted growth of plant organs. Phys Rev Lett. 2012;109(12):128104.

[55] Buschmann H, Borchers A. Handedness in plant cell expansion: a mutant perspective on helical growth. New Phytologist. 2020;225:53–56.

[56] Furutani I, Watanabe Y, Prieto R, Masukawa M, Suzuki K, Naoi K, et al. The *SPIRAL* genes are required for directional control of cell elongation in *Arabidopsis thaliana*. Development. 2000;127:4443–53.

[57] Nakamura M, Hashimoto T. A mutation in the Arabidopsis gamma-tubulin-containing complex causes helical growth and abnormal microtubule branching. Journal of Cell Science. 2009;122:2208–17.

[58] Thitamadee S, Tuchihara K, Hashimoto T. Microtubule basis for left-handed helical growth in Arabidopsis. Nature. 2002;417(6885):193–196.

[59] Sunohara H, Kawai T, Shimizu-Sato S, Sato Y, Sato K, Kitano H. A dominant mutation of TWISTED DWARF 1 encoding an α-tubulin protein causes severe dwarfism and right helical growth in rice. Genes & genetic systems. 2009;84(3):209–218.

[60] Ishida T, Kaneko Y, Iwano M, Hashimoto T. Helical microtubule arrays in a collection of twisting tubulin mutants of Arabidopsis thaliana. Proceedings of the National Academy of Science. 2007;104(20):8544–9.

[61] Buschmann H, Hauptmann M, Niessing D, Lloyd CW, Schäffner AR. Helical growth of the Arabidopsis mutant tortifolia2 does not depend on cell division patterns but involves handed twisting of isolated cells. The Plant Cell. 2009;21(7):2090–2106.

[62] Nakamura M, Naoi K, Shoji T, Hashimoto T. Low concentrations of propyzamide and oryzalin alter microtubule dynamics in Arabidopsis epidermal cells. Plant and cell physiology. 2004;45(9):1330–1334.

[63] Landrein B, Lathe R, Bringmann M, Vouillot C, Ivakov A, Boudaoud A, et al. Impaired cellulose synthase guidance leads to stem torsion and twists phyllotactic patterns in Arabidopsis. Curr Biol. 2013;23(10):895–900. doi:10.1016/j.cub.2013.04.013.

[64] Liu Z, Schneider R, Kesten C, Zhang Y, Somssich M, Zhang Y, et al. Cellulose-Microtubule Uncoupling Proteins Prevent Lateral Displacement of Microtubules during Cellulose Synthesis in Arabidopsis. Developmental Cell. 2016;38(3):305 – 315. doi:http://dx.doi.org/10.1016/j.devcel.2016.06.032.

[65] Saffer AM, Carpita NC, Irish VF. Rhamnose-containing cell wall polymers suppress helical plant growth independently of microtubule orientation. Current Biology. 2017;27(15):2248–2259.

[66] Chan J, Calder G, Fox S, Lloyd C. Cortical microtubule arrays undergo rotary movements in Arabidopsis hypocotyl epidermal cells. Nature Cell Biology. 2007;9(2):171–5.

[67] Verger S, Liu M, Hamant O. Mechanical conflicts in twisting growth revealed by cell-cell adhesion defects. Frontiers in plant science. 2019;10:173.

Supplementary Figures

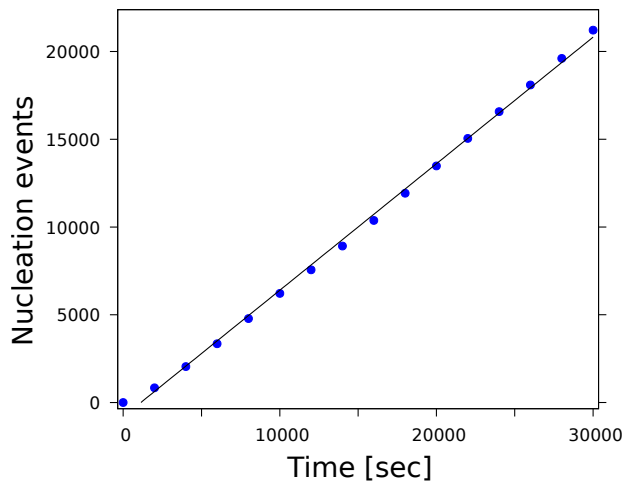

Figure S1: Cumulative number of nucleation events as a function of time for one simulation run with LDD nucleation mode and in a square simulation domain with periodic boundary conditions and size $L = 40\mu$m. The black line corresponds to the fitting function $f(t) = a + bt$, with $a = -809 \pm 153$ and $b = 0.72 \pm 0.01$. In this simulation, $r_c = 0.0025$ sec^{-1}.

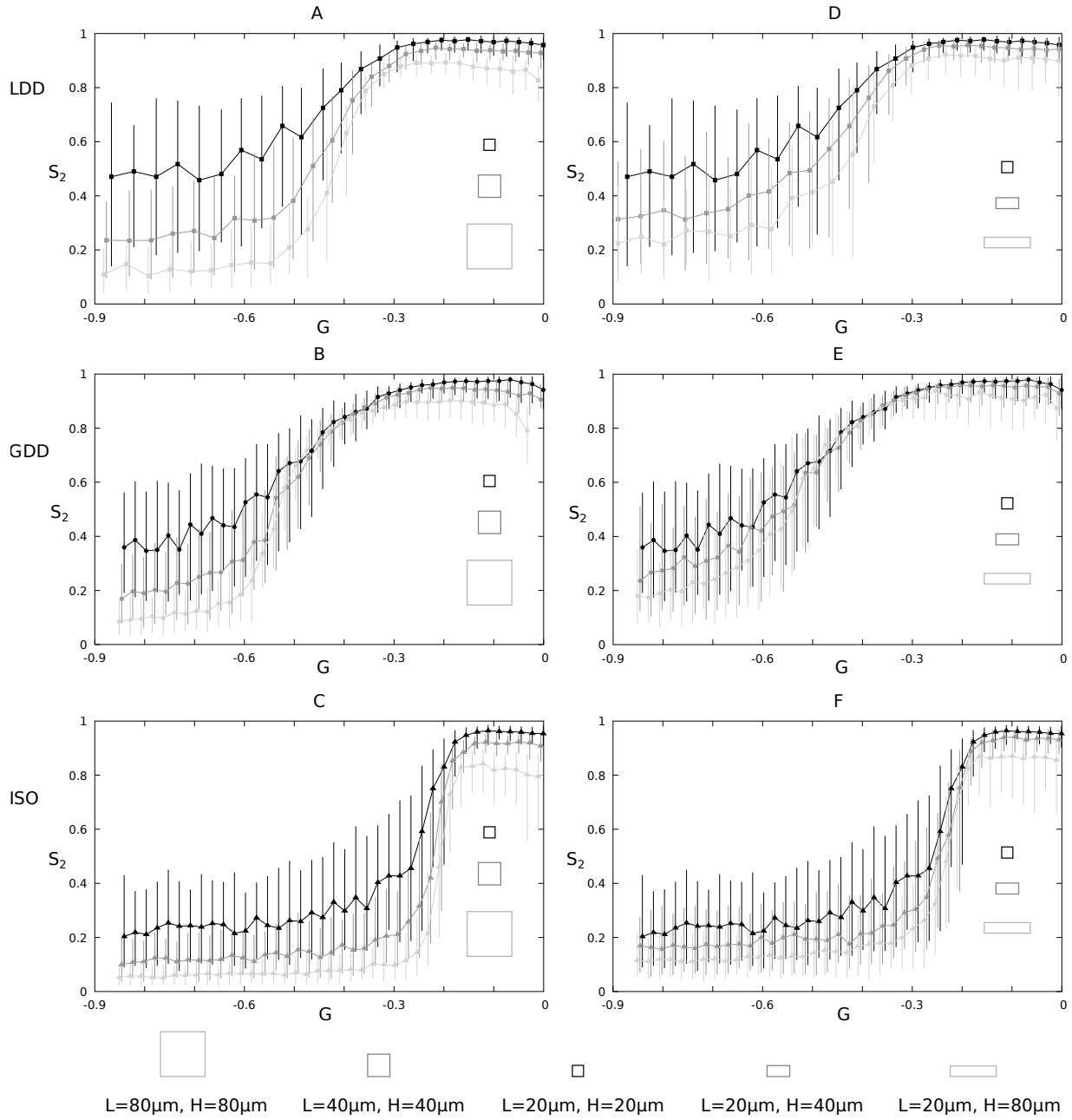

Figure S2: Degree of alignment S_2 as a function of the control parameter G for LDD, GDD, and ISO nucleation modes for (A-C) increasing size and (D-F) increasing height-to-length aspect ratio of the planar simulation domain. (B,C,E,F) In the ISO and GDD cases, results for the $L = 20\mu$m, $H = 20\mu$m grid are shifted to the right on the G axis by 0.005, whereas results for the $L = 80\mu$m, $H = 80\mu$m and the $L = 20\mu$m, $H = 80\mu$m grids are shifted to the left by 0.005 for visibility of the error bars. Error bars represent the 10th and 90th percentile.

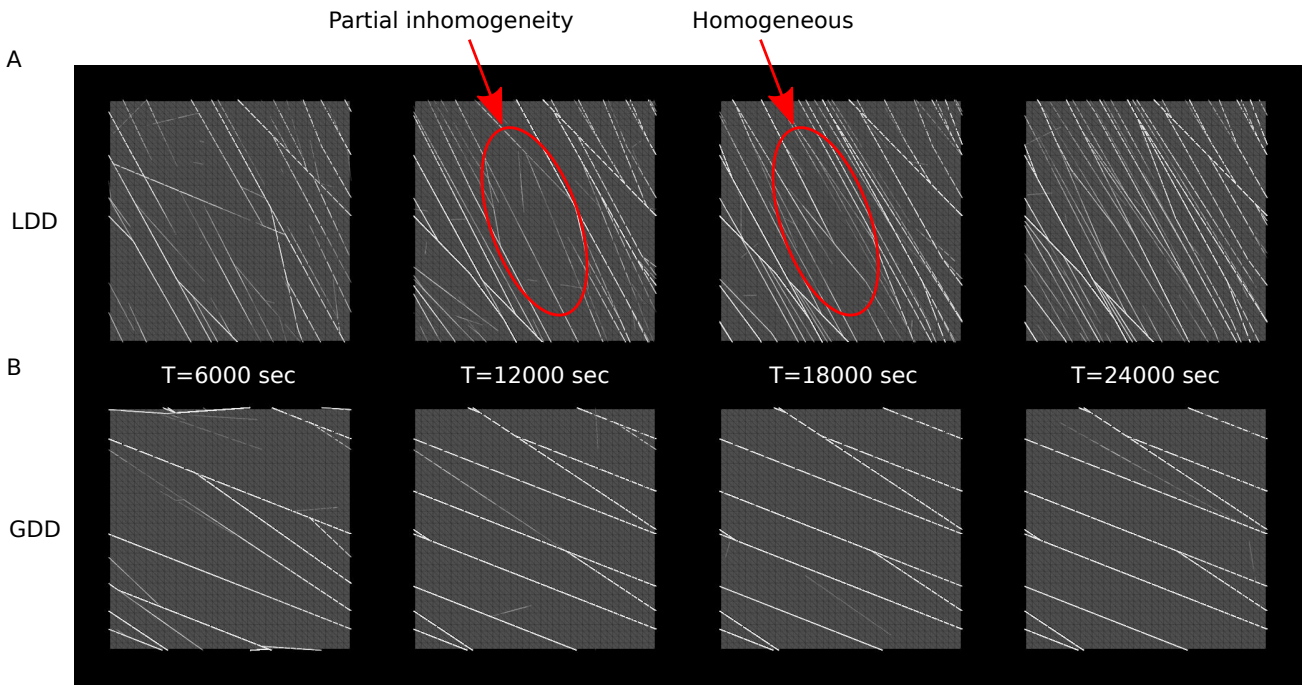

Figure S3: Snapshot of the simulated cortical array for (A) LDD and (B) GDD nucleation modes at four different time stamps. Ellipse in A indicate a region of initially low density where density increases over time. Simulation domain: grid $L = 40\mu$m, $H = 40\mu$m. $r_c = 0.0025$ s^{-1}.

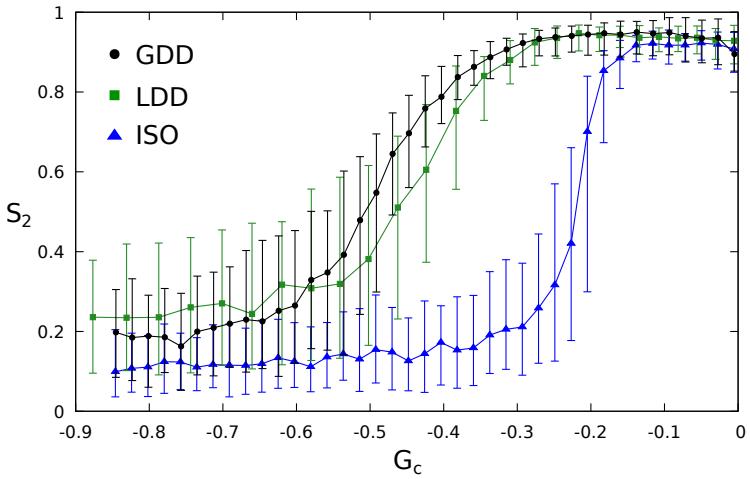

Figure S4: Order parameter S_2 as function of the control parameter G at $T = 3 \times 10^4$ sec, for LDD, GDD, and ISO nucleation modes in a squared geometry with sizes $L = 40\mu$m and $H = 40\mu$m, as depicted in Figure 4. Results are averaged over 100 independent simulation runs, and error bars represent the 10th and 90th percentile.

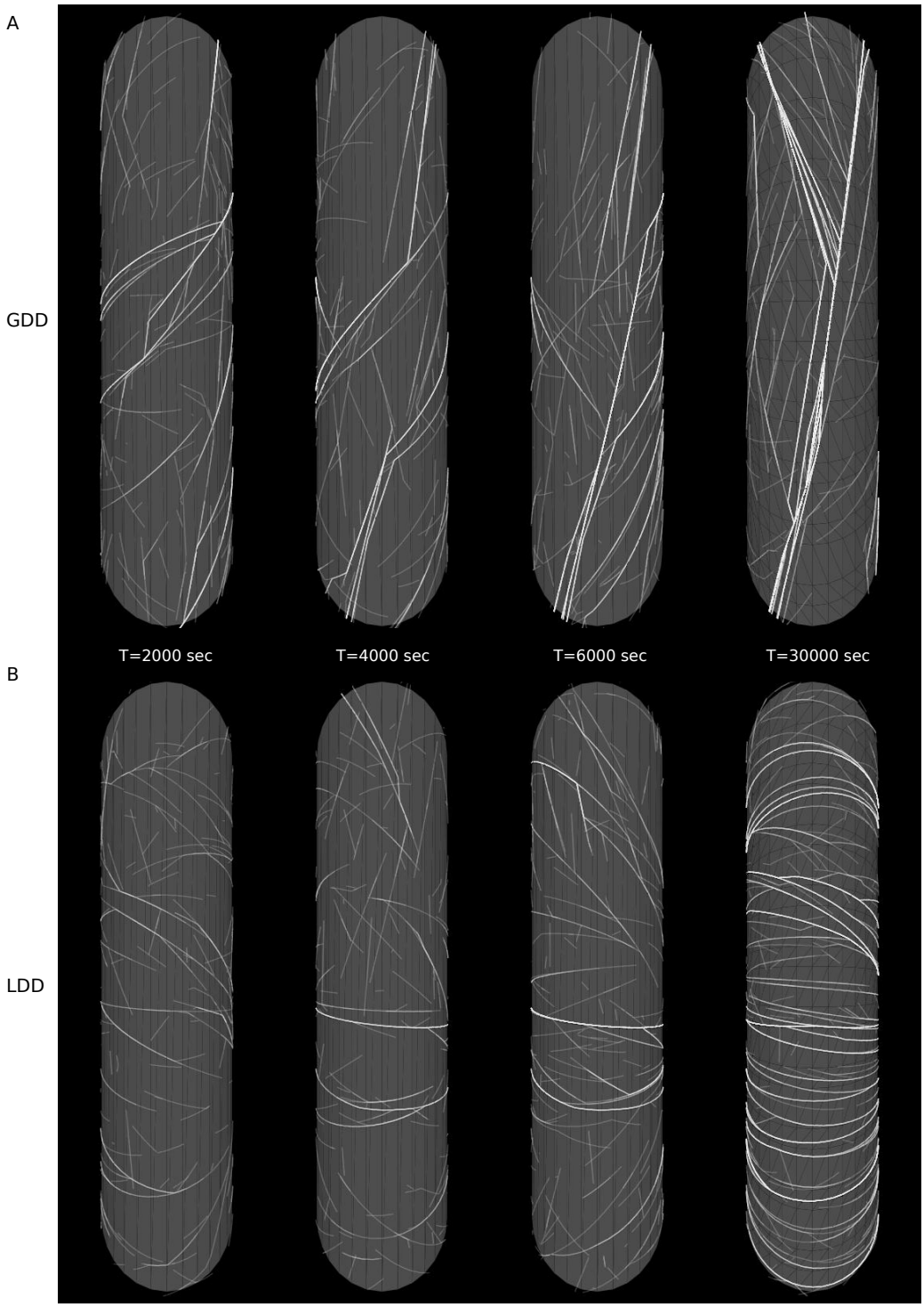

Figure S5: Snapshot of the simulated cortical array for (A) LDD and (B) GDD nucleation modes at four different time stamps. Simulation domain: cylinder with length= 40μm, diameter= 40μm. In these simulations: $r_c = 0.0025$ s^{-1}.